phys. stat. sol. (b) **226**, No. 1, 9–19 (2001)

Indirect Bandgap-Like Current Flow in Direct Bandgap Electron Resonant Tunneling Diodes

GERHARD KLIMECK[1])

Jet Propulsion Laboratory, California Institute of Technology, Pasadena, CA 91109, USA

(Received April 1, 2001; accepted May 1, 2001)

Subject classification: 71.20.Nr; 72.80.Ey; 73.20.At; 73.40.Gk; S7.12

The current turn-on and turn-off in a resonant tunneling diode (RTD) is determined by the crossing of the central resonance subband with the Fermi level in the emitter, the subbands of quasi-bound states in the emitter and the conduction band edge in the emitter. In a typical RTD the subbands in the central well and the emitter are similar, resulting in a simple resonant current flow for almost all transverse momenta. Since most of the electrons have zero transverse momentum, one therefore observes that most of the carriers travel straight through the structure. This paper presents a mechanism that can generate off-zone-center current flow in electron resonant tunneling diodes, where most of the carriers travel through the structure at an angle for a certain bias range. The basic idea is that if the effective mass in the RTD well is much smaller than the effective mass in the emitter, subband crossings will occur outside the zone center, resulting in this unintuitive distribution of the current as a function of transverse momentum. This mechanism is shown to increase the valley current within a single band approximation without non-parabolicity.

1. Introduction

1.1 Nanoelectronic modeling (NEMO)

The quantum mechanical functionality of devices such as resonant tunneling diodes (RTDs), quantum well infrared photodetectors, and quantum well lasers is enabled by material variations on an atomic scale. The creation of these heterostructure devices is realized in a vast design space of material compositions, layer thicknesses and doping profiles. The full experimental exploration of this design space is unfeasible and a reliable design tool is needed.

The Nanoelectronic Modeling tool (NEMO) is one of the first commercial grade attempts for such a modeling tool. NEMO was developed as a general-purpose quantum mechanics-based 1D device design and analysis tool from 1993–97 by the Central Research Laboratory of Texas Instruments (later Raytheon Systems). Free executables can be requested on the NEMO web site.[2]) NEMO enables the fundamentally sound inclusion of the required physics to study electron transport in RTDs: bandstructure, scattering, and charge self-consistency based on the non-equilibrium Green function approach. The theory used in NEMO and in this work is documented in Refs. [1–3] while some of the major simulation results are documented in Refs. [4–10]. NEMO development is presently continued at the Jet Propulsion Laboratory towards the modeling of light and THz detection and emission devices.

The work presented here was enabled by the implementation of parallelism in NEMO on simultaneous, various levels: voltage, transverse momentum integration, and energy integration. The use of massively parallel computers enabled the thorough ex-

[1]) email: gekco@jpl.nasa.gov.

[2]) See http://hpc.jpl.nasa.gov/PEP/gekco/nemo, or search for NEMO on http://www.raytheon.com.

 0370-1972/01/22607-0009 $ 17.50+.50/0

ploration of the state space in total energy E and transverse momentum k for a significant number of bias points.

1.2 Effects due to effective mass variations

Heterostructures such as resonant tunneling diodes can be technically realized by the deposition of different semiconductors on top of each other with (almost) atomically smooth interfaces. The built-in potential in these devices is dominated by the different bandgaps and band offsets in the adjoining materials, and these built-in potentials are used to construct barriers and wells. The associated spatial variations in the effective mass in the different materials are overall a secondary effect compared to the dramatic potential variations. However, effective mass variations need to be considered in careful simulations of resonant tunneling diodes. The basic effects of the effective mass on the separation of the RTD bound states[3]) and the wavefunction attenuation in the barriers[4]) are easily understood in single band effective mass models. Quantitative simulations of RTD current–voltage characteristics at high temperatures[5]) must include higher order bandstructure effects such as non-parabolicity and band warping [5–7]. In fact, the simple description of the bandstructure with a single conduction band edge and a single effective mass appears to break down completely for the detailed understanding of high performance RTDs. Such detailed analysis requires [7] that the in-plane (transverse to the layer sequence) degree of freedom of the electrons be treated explicitly with the transverse momentum k. The study of the electron flow as a function of the transverse electron momentum has led to the primary result in this paper: if the effective mass in the RTD well is smaller than the effective mass in the emitter, more electrons may travel at an angle through the structure rather than straight through the structure. In the simulations shown in this publication, only a simple effective mass model is used to avoid complications due to band non-parabolicity and to focus on the basic physics of dispersion crossings.

1.3 Overview of the paper

Sections 2 and 3 discuss approximations for calculating current density and detail our approach for explicitly including its dependence on transverse momentum. Section 4 provides a description of the RTD structure, the relevant energy scales, and the material parameters that are considered here. Section 5 discusses the basic physics of the origin of the off-zone-center current flow that is the central theme of this paper. Section 6 presents the consequences of the off-zone-center current flow on the overall

---

[3]) In an infinite barrier square well of width a the energy separation is

$$\Delta E_{n+1} = E_{n+1} - E_n \propto \hbar^2\pi^2/2ma^2 \propto 1/m$$

when described by a single effective mass.

[4]) For a single square barrier of thickness d the exponential $e^{-\kappa d}$ decay constant is defined as $\kappa = \sqrt{2m\,\Delta E/\hbar^2} \propto \sqrt{m}$ if described by a single band model.

[5]) At low temperatures it has been found that the non-parabolic bandstructure shows negligible effects versus effects from incoherent scattering with phonons and material disorder [5, 7–10]. On the contrary it has been found that such incoherent scattering effects are negligible in RTD electron transport at high temperatures [5–7].

current–voltage characteristics. Finally, some of the limitations of the model used here are discussed in Section 7.

2. Current Density J(k)

It has been shown that for typical high performance RTDs used in memory [11] and logic [12] circuits operated at room temperature, the effects of incoherent scattering inside the central RTD region [5, 8–10] are negligible while bandstructure effects such as non-parabolicity and complex band wrapping are dominant [5–7]. In such a case, the current can be computed [1, 7] using an expression of the form:

$$J \propto \int \mathrm{d}E \int k \,\mathrm{d}k\, \mathcal{T}(E,k)\,(f_{\mathrm{L}}(E) - f_{\mathrm{R}}(E)) \tag{1}$$

$$= \int \mathrm{d}E \int k \,\mathrm{d}k\, J(E,k)\,, \tag{2}$$

where k is the electron momentum transverse to the transport direction normalized to the unit cell a by $\frac{\pi}{a}$, E is the total energy, $\mathcal{T}$ is the transmission coefficient, and $f_{\mathrm{L/R}}$ is the Fermi function in the left/right contact.

Since transmission coefficient $\mathcal{T}(E,k)$ may contain sharp resonances (10^{-9}–10^{-3} eV) that have to be resolved very well in an energy range of typically 1 eV, it may be expensive to compute. NEMO contains algorithms that locate [13] and resolve [14] the resonances for a constant transverse momentum k. It is therefore convenient for numerical reasons to reverse the order of integration in Eq. (2) and to define an intermediate quantity $J(k)$ as follows:

$$J(k) = \int \mathrm{d}E\, J(E,k) \tag{3}$$

such that

$$J \propto \int k \,\mathrm{d}k\, J(k)\,. \tag{4}$$

Not only is this quantity $J(k)$ numerically convenient, but it also bears physical insight as to "where" the carrier transport occurs in k-space. This paper stems from the analysis of the distribution of $J(k)$ as a function of transverse momentum k and applied voltage.

3. Tsu-Esaki Formula

A common approach in reducing the required CPU time needed to compute a complete I–V characteristic is the assumption of parabolic transverse subbands such that the transmission coefficient has an analytic, parabolic transverse momentum dependence: $\mathcal{T}(E,k) = \mathcal{T}(E - \hbar^2 k^2/2m^*,\, k=0)$. Under this assumption the transverse momentum integration in Eq. (1) can be carried out analytically to result in the so-called Tsu-Esaki [15] formula:

$$J \propto \rho_{2\mathrm{D}} \int \mathrm{d}E\, \mathcal{T}(E, k=0) \ln\left(\frac{1 + \mathrm{e}^{(E_{\mathrm{F}} - E)/kT}}{1 + \mathrm{e}^{(E_{\mathrm{F}} - E - qV)/kT}}\right). \tag{5}$$

The Tsu-Esaki 1D integration formula is capable of providing qualitatively correct results for electron devices given the restrictive assumption that subband alignment is

not the primary transport mechanism [7, 16–18]. Technologically relevant RTDs that show negative differential resistance at room temperature all exhibit a triangular emitter well such that there is a large 2D to 2D subband tunneling contribution from emitter to central resonance. To achieve quantitative agreement [6, 7] between simulation and experimental data for such RTDs, full 2D integrations in energy E and transverse momentum k according to Eq. (2) must be performed. In fact, the limitations of the Tsu-Esaki formula have been discussed previously for direct bandgap electron systems [5, 7, 16, 17], intra band systems [19, 20] and hole transport systems [21–24]. The main effect of the breakdown of the Tsu-Esaki approximation in the structure simulated in this publication is an under-estimate of the valley current in the RTD.

4. RTD Structure and Simulation Details

The InP-based RTD considered here has been studied experimentally in Ref. [25]. The emitter and collector consist of $In_{0.53}Ga_{0.47}As$, and the barriers are seven monolayers (ML) of pseudomorphic AlAs. The well consists of three layers: 8 ML of InAs surrounded by 5 ML of InGaAs. The central RTD is contacted with a 2 nm undoped spacer, a 50 nm low doping region ($10^{18}\,cm^{-3}$) and a 50 nm high doping region ($5 \times 10^{18}\,cm^{-3}$) symmetrically around the RTD.

Figure 1 shows a segment of the conduction band edge around the central RTD region and some critical energies at a bias of 0.3 V. The energy scales are chosen such that the flatband emitter energy is at zero energy with a Fermi energy at about 252 meV in the high doping region. The low doping region connected to the high doping region causes a built-in potential of about 170 meV. The Fermi levels in the emitter

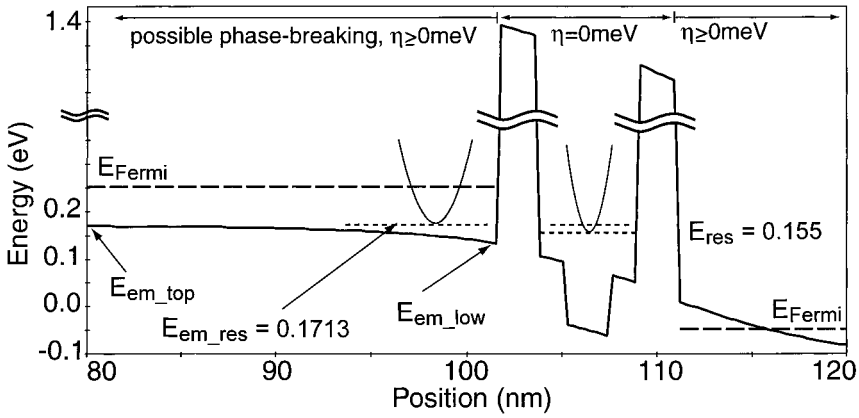

Fig. 1. Conduction band profile of the RTD at a bias of 0.3 V (solid line). Fermi levels in the emitter and collector are indicated by long dashed lines. Resonances in the quantum well at 0.155 eV and emitter at 0.1713 eV are indicated with short dashed lines. The emitter quasi bound state is strongly coupled to the central resonance, resulting in a wavefunction contribution in the quantum well. The largest energy in the emitter over which propagating states can travel from the emitter is indicated as $E_{\mathrm{em\_top}}$. The minimum energy in the triangular emitter well is labeled as $E_{\mathrm{em\_low}}$. The dispersions in the transverse directions in the emitter and the quantum well are shown by the two parabolas with different curvatures. The vertical energy scale is contracted as indicated by the double wavy lines. Emitter and collector regions are assumed to be in local equilibrium and characterized by a phase-breaking potential $\eta \geq 0$ eV. The central RTD region never contains such a self-energy ($\eta = 0$ eV) in the simulations shown here

and the collector are indicated as horizontal dashed lines. The boundary conditions developed [1, 4] for NEMO assume that the emitter and the collector are in local equilibrium. The non-equilibrium region is typically set such that carriers are injected into the central device region at the beginning of the first barrier (see the arrow labeled $E_{\mathrm{em\_low}}$). The transmission coefficient $\mathcal{T}(E,k)$ does contain information about the quasi-bound states in the emitter [1, 4] below the energy $E_{\mathrm{em\_top}}$ as well as the continuum states above that critical energy. Therefore, carrier injection from the continuum states above the critical energy and from the quasi-bound states $E_{\mathrm{em\_res}}$, is included in the simulation. The empirical scattering rate $\eta = \frac{\hbar}{2\tau}$ describes the filling of the states that are quasi-bound in the emitter under the critical energy $E_{\mathrm{em\_top}}$. It has been shown that the current through the RTD may be strongly dependent on that scattering rate for particular structures [26]. The simulations shown in this paper will compare two different cases with respect to the choice of η: (i) $\eta = 0$ meV, no scattering in the emitter, and (ii) $\eta = 6.6$ meV ($\tau \approx 0.05$ ps) a typical [4, 6, 7] value for η.

The simulations discussed in this paper use a simple single band model to show the importance of subband crossing and to avoid detailed issues such as the correct non-parabolicity under strain. The single band model is completely parameterized by band offsets and effective masses[6]): $\Delta E_{\mathrm{InGaAs}} = 0.0$ eV, $m^*_{\mathrm{InGaAs}} = 0.044$, $\Delta E_{\mathrm{AlAs}} = 1.839$ eV, $m^*_{\mathrm{AlAs}} = 0.09$, $\Delta E_{\mathrm{InAs}} = -0.192$ eV, $m^*_{\mathrm{InAs}} = 0.024$. The potential profile is based on a semi-classical self-consistent charge distribution. A semi-classical charge based on a linearly interpolated Fermi level in the center of the RTD is included since the InAs notch in the center of the RTD lowers the bandedge significantly and contains significant charge in the center of the well. The simulations presented here compare four different simulations: zero or non-zero η, combined with current density evaluations according to Eq. (1) or Eq. (5). Since the current distributions will be shown to differ for these four simulations, one can infer different charge distributions and Hartree potential corrections as well, therefore resulting in different dispersion alignments. Since the focus of this paper is to explain basic transport mechanism of subband alignment and not detailed comparisons of charge distribution effects, no Hartree self-consistency is included here and the same semi-classical charge self-consistent potential is used in all four simulations.

A word of caution about the validity of these simple single band simulations can be found in Section 7 towards the end of the paper.

The next section discusses the line-ups of the central resonance, the emitter resonance, the lowest emitter bandedge, and the topmost emitter bandedge. It is noted here that, within the simple effective mass model and the simple semi-classical potential model, the emitter resonance $E_{\mathrm{em\_res}}$ aligns with the top of the emitter $E_{\mathrm{em\_top}}$ within the resonance linewidth for biases greater than 0.2 V (i.e., $E_{\mathrm{em\_res}} \approx E_{\mathrm{em\_top}}$) for this particular device.

5. Off-Center Current Flow

Figure 2 provides a physical picture of the off-zone-center current flow in direct bandgap semiconductors. The middle row shows the quantum well dispersion (solid line),

[6]) The effective mass in AlAs is reduced from its bulk value to achieve a reasonable transparency of the barrier due to band wrapping to the valence band [7].

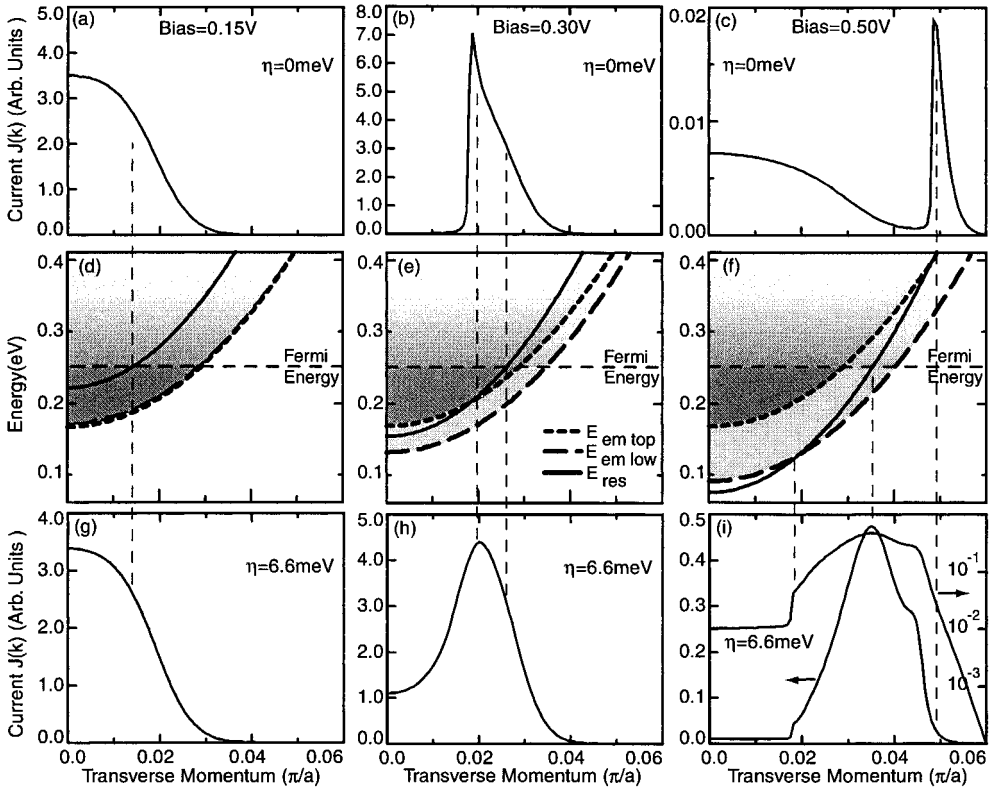

Fig. 2. First row (a–c): Current density $J(k)$ as a function of momentum at three different biases (0.15, 0.3, and 0.5 V) without any phase-breaking in the emitter. Second row (d–f): Electron dispersions as a function of transverse momentum, $E(k)$, for the quantum well resonance (E_{res}, solid line), the bottom of the emitter ($E_{\mathrm{em\_low}}$, long dashed line), and the top of the emitter ($E_{\mathrm{em\_top}}$, short dashed line). The Fermi level in the emitter is indicated by a horizontal thin dashed line. Filling of the emitter dispersions $E_{\mathrm{em\_low}}$, $E_{\mathrm{em\_top}}$ is indicated by dark and light gray areas, respectively. Third row (g–i): same as first row but with a finite phase-breaking energy of 6.6 meV. (i) shows $J(k)$ also on a logarithmic scale (inner right scale). First column (a, d, g): bias of 0.15 V; second column (b, e, h): bias of 0.3 V; third column (c, f, i): bias of 0.5 V

two dispersions in the emitter ($E_{\mathrm{em\_top}} = E_{\mathrm{em\_res}}$, short dashed line; and $E_{\mathrm{em\_top}}$, long dashed line) and the Fermi level in the emitter (horizontal dashed line) for three different biases (0.15, 0.3, and 0.5 V). The electron supply from the emitter bound state, as well as the bottom of the 3D emitter, are indicated by dark and light gray shades, respectively. Note that the Fermi sea is not sharply cut off, as indicated by the dashed line; however, there is a significant number of excited carriers above the Fermi sea due to thermal excitation at 300 K, as indicated by the decreasing shading with increasing energy.

The first row of Fig. 2 depicts the current densities $J(k)$ as a function of transverse momentum at the different biases. At a bias of 0.15 V, $J(k)$ is a smooth monotonically decreasing function, as typically expected [22, 24] in RTDs. In typical RTDs such monotonic behavior is expected for all bias points. In fact, it has been analytically shown [22] that $J(k)$ is always peaked at $k = 0$ if the emitter and the well effective mass are the same.

At higher biases of 0.3 and 0.5 V, sharp turn-ons in $J(k)$ can be seen. These sharp turn-ons are associated with the crossing of the central quantum well resonance, E_{res}, with the emitter quasi-bound state, $E_{\mathrm{em\_res}} \approx E_{\mathrm{em\_top}}$. The peak in $J(k)$ occurs at the crossing of the dispersion. The smooth turn-offs of $J(k)$ are associated with the decrease of thermally (300 K) excited carriers above the Fermi energy.

At 0.5 V applied bias the current density $J(k)$ shows a sharp peak at $k \approx 0.05$, which corresponds to the subband crossing 150 meV above the Fermi energy. Few carriers are available at such high energies, and the current contribution at that large momentum is small.

The first two rows of Fig. 2 show a clean example of dispersions that can lead to non-monotonic, sharply spiked, current density distributions $J(k)$ as a function of momentum. If $J(k)$ is at a maximum away from $k = 0$, as indicated in the two cases of 0.3 and 0.5 V, and if the first moment $k_J = \frac{\int \mathrm{d}k\, kJ(k)}{\int \mathrm{d}k\, J(k)}$ of the distribution $J(k)$ is close to the peak $k_{\max} = \max(J(k))$, as expected at 0.3 V it can be argued that most of the carriers travel off the zone center at Γ. In other words, more carriers travel at an angle through the structure rather than straight through the structure.

The lower panel in Fig. 2 (g–i) shows the effect brought about by the introduction of a finite phase-breaking in the emitter of $\eta = 6.6$ meV compared to $\eta = 0$ eV in the upper panel. There is little difference between Figs. 2a and g while there are significant differences between Figs. 2b and h and Figs. 2c and i. Figure 2h appears to be a smoothed version of Fig. 2b with a finite current contribution before the current turn-on at $k < 0.02$. That current contribution can be attributed to tunneling out of states above the bottom of the emitter (long dashed line, $E_{\mathrm{em\_low}}$) that are broadened by the phase-breaking η. Within NEMO the phase-breaking self-energy $\eta(z, E, k)$ is typically treated as a function of space (growth direction z), total energy E and momentum k. η is assumed constant above the conduction band $E(z, k)$ and exponentially decaying below it. The exponential decay rate is typically chosen to be identical to η. A reduction of this decay rate to 1 μeV has been verified (not shown here) to reduce the current slightly.

Figure 2i shows the distinction for tunneling out of the bottom emitter states and the resonant emitter states more clearly. There is a distinct turn-on in $J(k)$ as the quantum well resonance dispersion crosses the bottom of the emitter dispersion at $k \approx 0.018$. The coupling to the broadened emitter resonance (short dashed line) gets stronger for increasing momentum, and the current $J(k)$ keeps increasing. As the quantum well resonance dispersion crosses the Fermi level, the number of carriers starts to decrease with energy significantly, and $J(k)$ starts to decrease significantly.

From the discussion of the physics in Fig. 2, it is clear that the lighter mass in the center of the RTD versus the mass in the emitter can lead to off-zone current flow. The next section will discuss how large the bias range might be in which such phenomena might occur and the effects on the current–voltage characteristics.

6. Current–Voltage Characteristics

Figure 3a shows the current density $J(k, V)$ as a function of transverse momentum and applied voltage on a gray scale contour plot. Dark shades indicate large current densities. The vertical lines in Fig. 3a correspond to the three cuts of $J(k)$ plotted in Fig. 2a–c for the three constant voltages 0.15, 0.3, and 0.5 V. If the dispersions in the emitter and

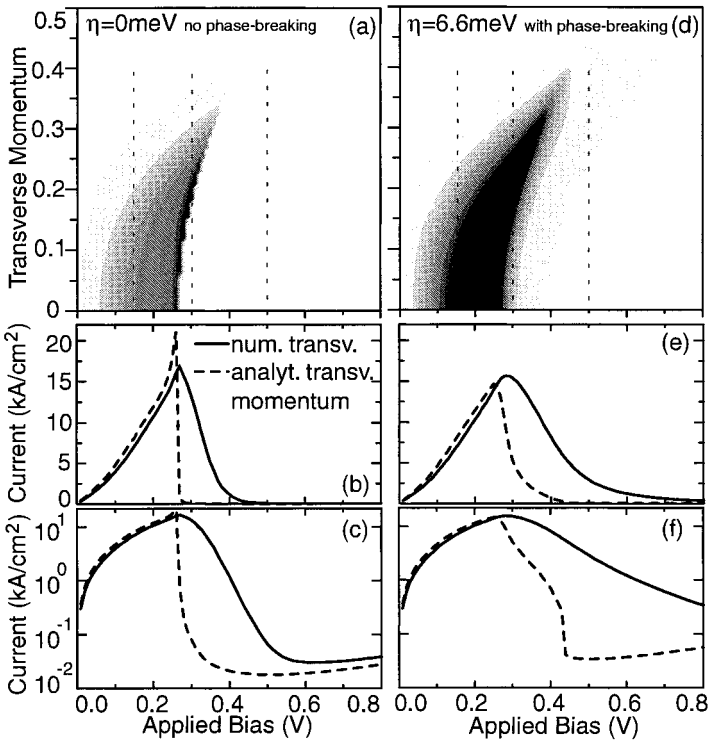

Fig. 3. (a) Current density $J(k, V)$ as a function of transverse momentum k and applied voltage V on a linear gray scale plot for zero emitter phase-breaking ($\eta = 0$ eV). Dark shades correspond to large values. Vertical dashed lines correspond through cuts of $J(k, V)$ for constant voltages as displayed in Figs. 2a–c. (b) I–V characteristic computed without (dashed line) and with (solid line) explicit numerical integration over the transverse momentum. Dashed line corresponds also to a cut along the voltage axis for $k = 0$ in (a). (c) Same as (b) but on a logarithmic scale. (d, e, f) Same as (a, b, c) except for non-zero phase-breaking in the emitter $\eta = 6.6$ meV

the central quantum well were identical and parabolic (in the energy range that transport occurs in), a sharp cut-off in the gray current density for *one* voltage [24] (here at about 0.28 V) would be seen. The different emitter and quantum well dispersions considered here, however, distribute the sharp current peak turn-on and turn-off along a parabolic distribution. It can be shown for holes at low temperatures that the $J(k, V)$ distribution starts to represent the $E(k)$ distribution [22, 23]. On the linear gray scale shown in Fig. 3a off-zone-center current flow can be identified for biases in the range of 0.28–0.4 V. The detailed plot of Fig. 2c actually shows a small off-zone-center current at a bias of 0.5 V.

Figure 3b shows the numerical integral of $J(k, V)$ corresponding to Eq. (1) in a solid line. The current based on the analytical transverse momentum integration (Tsu-Esaki approximation, Eq. (5), dashed line) ignores any spectral features in $J(k)$ as a function of momentum k and, therefore, fails to capture the off-zone-center current flow. The dashed line can also be considered a cut through Fig. 3a at zero transverse momentum $k = 0$. The numerical integration eliminates the unphysical current overshoot at the peak voltage 0.28 V that has previously been discussed in Refs. [5, 7, 17]. The numeri-

cal integration also captures the off-zone-center current flow that leads to an increased valley current through the device. That increased valley current is more dramatically visible on the logarithmic scale in Fig. 3c. Note that the simulation shown in the first column of Fig. 3 (a–c) does *not* contain any phase-breaking ($\eta = 0$). The crossing dispersions due to the lighter quantum well mass versus the emitter mass result in a significantly increased current flow in the valley current region.

The second column of Fig. 3 is based on an inclusion of phase-breaking of $\eta = 6.6$ meV and shows the equivalent data to the first column at $\eta = 0.0$ meV. The broadening in the emitter increases the number of momenta that can couple to the central resonance, as discussed in Figs. 2g–i. This broadening results in a further increased current flow in the valley current region.

Such an increased valley current can also be produced by a phase-breaking potential that is *not* energy dependent. Such a potential would essentially enable coupling of the central resonance to evanescent states in the emitter under the bandgap. It is pointed out here explicitly that this is *not* the case in these simulations. The increased valley current is due to the crossing of lighter effective mass central resonance dispersion with the heavier mass emitter dispersion as discussed in Figs. 2g–i. The current voltage characteristic based on the Tsu-Esaki approximation (dashed line) underestimates the valley current by several orders of magnitude.

Since the Tsu-Esaki approximation ignores the off-zone-center current flow completely, the voltage range in which off-zone-center current flow is important can be determined from the difference of the two current–voltage characteristics. In the $\eta = 0$ case it extends from 0.28 V to approximately 0.55 V, while in the $\eta = 6.6$ eV case it extends to voltages higher than 0.8 V.

7. Discussion

It is noted here that the purpose of this paper is not to compare to experimental data directly but to explain a novel physical effect in the electron transport through heterostructures. The off-zone-center current flow is shown to be purely due to the crossing of the lighter mass central resonance dispersion with the heavier mass emitter dispersion. We have explored one candidate structure in which this effect might occur. Such different mass configurations can be found in several other RTD structures, for example (i) an InP emitter with an $In_{0.53}Ga_{0.47}As$ well or (ii) a GaAs emitter with an $In_{0.14}Ga_{0.86}As$ well. The use of ternary alloys in laser and detector structures opens another wide design space in which such dispersion crossings and associated transport phenomena might occur.

The physical effect of off-zone-center current flow is determined solely by the crossing of the quantum well dispersion over the emitter dispersion at the turn-off region of the RTD. The conditions at which such a crossing occurs and the exact point in momentum space where this crossing occurs depends on the interplay between band offsets and effective masses. The crossing of the bands as described in Fig. 2 is necessary for the current flow; however, the presence of carriers at these energies is just as necessary. These arguments show that the presence of significant off-zone-center current flow can be seen as a fortuitous coincidence of band alignments, effective masses and Fermi levels. In hole RTDs, however, there is no dependence on band offsets, since the heavy and light hole band are already at the same energy. In these systems it can be shown [22, 23] that off-zone-center current flow should occur in almost any structure.

The simulations shown here are performed with a simple one-band model to illustrate the physical effect of a smaller quantum well mass versus the emitter mass on the electron transport. The $I-V$ characteristics shown here have the same current peak amplitude found in the experimental data [25]; however, the peak voltage in the experiment is at about 0.18 V, and the turn-on of the second peak occurs at about 0.4 V versus the 0.4 and 0.8 V, respectively, shown in the simulations. The quantitative modeling of RTDs that include InAs central notches is made difficult by the correct modeling of the strained InAs. The exact non-parabolicity and the band offsets of the InAs in this strained system is still under investigation. InAs is known to exhibit strong non-parabolicity, which is expected to modify the details of the dispersions shown here. Preliminary simulations of these structures in a full band sp3s* bandstructure model use an empirically fit InAs bandstructure and indicate that the voltage region in which off-zone-center current occurs may be reduced significantly. However, the increased valley current is being seen in those preliminary simulations. The simple bandstructure model used here does not show any non-parabolicity in the energy ranges that are considered here and, therefore, clearly over-estimates the effects of the off-zone-center current in the valley current region.

The author would like to point out that he has observed such off-zone-center current flow in electron transport simulations for a variety of different structures in the past, including bandstructure models that contain band non-parabolicity. Such occurrences have typically wreaked havoc in the simulations since the number of numerical k-points that are typically specified in the algorithm to resolve the expected smooth curve shown in Fig. 2a is much smaller than the number of points needed to resolve Fig. 2b. Detailed numerical integration over the transverse momentum was prohibitively expensive before the parallelization of NEMO. Only with the analytical expressions published in Ref. [22], this sharply spiked behavior of $J(k)$ was understood.

In attempts to simulate electron transport in structures with strongly varying effective masses that is subject of incoherent scattering, careful attention should be given to the distribution of carriers in momentum space, the subband crossings between emitter states, and central resonance states and the momentum transfer by phonons.

8. Summary

This paper describes a mechanism that may contribute to an enhanced valley current in high performance RTDs. This mechanism is uncovered in the detailed analysis of the RTD current flow as a function of the transverse momentum. The dependence on this additional degree of freedom is often neglected by the use of the Tsu-Esaki formula. While some of the limitations of the Tsu-Esaki approximation are only exposed in higher fidelity bandstructure models that contain band non-parabolicity, the break-down of the Tsu-Esaki formula is demonstrated here for even the most simple single-band effective mass bandstructure model. The basic mechanism relies on the crossing of the central resonance dispersion (light mass) with the emitter dispersion (heavier mass) at a momentum value greater than zero in the turn-off region of the RTD. In such a situation, more electrons may flow through the structure with non-zero transverse momentum than with zero transverse momentum. This implies that the current transport becomes indirect bandgap-like.

Acknowledgements The work described in this publication was carried out at the Jet Propulsion Laboratory, California Institute of Technology under a contract with the National Aeronautics and Space Administration. The supercomputer used in this investigation was provided by funding from the NASA Offices of Earth Science, Aeronautics, and Space Science. I would also like to acknowledge the careful review of the manuscript by Dr. Timothy B. Boykin and fruitful previous collaborations that lead up to this work within the NEMO team consisting of Dr. R. Chris Bowen, Dr. Roger Lake and Dr. Timothy B. Boykin.

References

[1] R. Lake, G. Klimeck, R. C. Bowen, and D. Jovanovic, J. Appl. Phys. **81**, 7845 (1997).
[2] R. Lake, G. Klimeck, R. Bowen, D. Jovanovic, and D. Blanks, phys. stat. sol. (b) **204**, 354 (1997).
[3] T. B. Boykin, L. J. Gamble, G. Klimeck, and R. C. Bowen, Phys. Rev. B **59**, 7301 (1999).
[4] G. Klimeck, R. Lake, R. C. Bowen, W. R. Frensley, and T. Moise, Appl. Phys. Lett. **67**, 2539 (1995).
[5] R. Lake, G. Klimeck, R. C. Bowen, C. Fernando, D. Jovanovic, D. Blanks, T. S. Moise, Y. C. Kao, M. Leng, and W. R. Frensley, in: 54th Annual Device Research Conf. Digest, IEEE, NJ, 1996 (p. 174).
[6] G. Klimeck, T. B. Boykin, R. C. Bowen, R. Lake, D. Blanks, T. S. Moise, Y. C. Kao, and W. R. Frensley, in: 55th Annual Device Research Conf. Digest, IEEE, NJ, 1997 (p. 92).
[7] R. C. Bowen, G. Klimeck, R. K. Lake, W. R. Frensley, and T. Moise, J. Appl. Phys **81**, 3207 (1997).
[8] R. Lake, G. Klimeck, R. C. Bowen, C-J. Fernando, M-H. Leng, T. Moise, and Y. C. Kao, Superlattices Microstruct. **20**, 279 (1996).
[9] R. Lake, G. Klimeck, and D. K. Blanks, Semicond. Sci. Technol. **13**, A163 (1998).
[10] G. Klimeck, R. Lake, and D. K. Blanks, Phys. Rev. B. **58**, 7279 (1998).
[11] J. P. A. van der Wagt, Alan C. Seabaugh, and E. Beam III, IEEE Electron Device Lett. **19**, 7 (1998).
[12] T. P. E. Broekaert, B. Brar, J. P. A. van der Wagt, A. C. Seabaugh, T. S. Moise, F. S. Morris, E. Beam III, and G. A. Frazier, IEEE J. Solid State Electron. **33**, 1342 (1998).
[13] R. C. Bowen, W. R. Frensley, G. Klimeck, and R. K. Lake, Phys. Rev. B **52**, 2754 (1995).
[14] G. Klimeck, R. Lake, R. C. Bowen, C-J. L. Fernando, and W. R. Frensley, VLSI Des. **6**, 107 (1998).
[15] R. Tsu and L. Esaki, Appl. Phys. Lett. **22**, 562 (1973).
[16] T. B. Boykin, R. E. Carnahan, and R. J. Higgins, Phys. Rev. B **48**, 14232 (1993).
[17] T. B. Boykin, R. E. Carnahan, and K. P. Martin, Phys. Rev. B **51**, 2273 (1995).
[18] T. B. Boykin, J. Appl. Phys. **78**, 6818 (1995).
[19] M. S. Kiledjian, J. N. Schulman, K. L. Wang, and K. V. Rousseau, Phys. Rev. B **46**, 16012 (1992).
[20] T. B. Boykin, Phys. Rev. B **51**, 4289 (1995).
[21] M. S. Kiledjian, J. N. Schulman, K. L. Wang, and K. V. Rousseau, Surf. Sci. **267**, 405 (1992).
[22] G. Klimeck, R. C. Bowen, and T. B. Boykin, Superlattices Microstruct. **29**, 187 (2001).
[23] G. Klimeck, R. C. Bowen, and T. B. Boykin, Phys. Rev. B **63**, 195310 (2001).
[24] G. Klimeck, R. C. Bowen, and T. B. Boykin, in: IEEE Proc., Internat. Conf. on Compound Semiconductors, accepted for publication (2000).
[25] T. S. Moise, Y.-C. Kao, A. J. Katz, T. P. E. Broekaert, and F. G. Celii, J. Appl. Phys. **78**, 6305 (1995).
[26] R. Lake, G. Klimeck, R. C. Bowen, D. Jovanovic, P. Sotirelis, and W. R. Frensley, VLSI Des. **6**, 9 (1998).